Percolating conductive networks in multiwall carbon nanotube-filled polymeric nanocomposites: towards scalable high-conductivity applications of disordered systems†

Alexander J. Wang, [ID] *[a] Kang-Shyang Liao,[a] Surendra Maharjan, [ID] [a] Zhuan Zhu,[b] Brian McElhenny,[a] Jiming Bao[b] and Seamus A. Curran[a]

Disordered polymeric composite systems ordinarily exhibit poor bulk electronic transport properties, restricting their use to low-conductivity applications. In this work, highly electroconductive multi-walled carbon nanotube (MWCNT)/polyurethane (PU) nanocomposites were assembled *via* an aqueous solvent-blending method. Low percolation thresholds of 0.001 wt% and 0.093 wt% were obtained using pristine MWCNTs (P-MWCNTs) and mildly oxidized MWCNTs (O-MWCNTs), respectively. Corresponding critical values of dimensionality of 2.067 ± 0.094 and 2.304 ± 0.114 were calculated for P-MWCNT/PU and O-MWCNT/PU composites, respectively, strongly suggesting the formation of three-dimensional percolating conductive networks permeating the PU host matrix above the percolation threshold. Saturated direct current conductivities as high as 839 ± 72 S cm^{-1} were measured for O-MWCNT/PU composites at a filler-loading of 30.9 wt%. MWCNT/PU composite surfaces functionalized with superhydrophobic perfluoroalkyl moieties *via* chemical vapor deposition of (tridecafluoro-1,1,2,2-tetrahydrooctyl)trichlorosilane exhibited sessile contact angles as high as 154° without adversely affecting electroconductivity.

Introduction

Disordered conductive systems (*e.g.*, polymer nanocomposites, conjugated polymers, and amorphous inorganic semiconductors) are assuming a more central role in modern electronics as demand for conductive, flexible, robust, and easily-processable materials increases.[1,2] This follows in part from recent work on disordered conjugated polymer systems demonstrating higher charge carrier mobility than their polycrystalline semiconductor analogs.[3–5] Filler-loaded polymer nanocomposites are compound materials comprised of functional nanostructures distributed throughout a structural host-polymer matrix.[6,7] Generally, the properties of a nanocomposite are an amalgam of the properties of the individual components. The tailorable functionalities of a nanocomposite typically follow from careful selection of a suitable nanostructure and optimization of the interfacial interactions between the nanostructure and host-polymer. Sumio Iijima's discovery of carbon nanotubes (CNTs) marked the beginning of a prolific research campaign centered on delineating the properties and applications of conjugated helical, tubular graphitic nanomaterials.[8–13] With pragmatic applications of isolated CNTs still in its infancy, a considerable measure of effort has been afforded to exploring the unique properties and applications of CNT/polymer nanocomposites.[14–22] Refinement of state-of-the-art synthesis techniques has translated to marked improvement in intra- and inter-batch control over CNT chirality, geometry, and purity, paving the way for more systematic and reproducible production of CNT-based nanocomposites at larger scales.

From an environmental/ecological standpoint, particularly at larger production scales, predominantly aqueous solutions that could effectively deagglomerate and uniformly disperse either functionalized or as made CNTs is ideal. However, the inherent hydrophobicity of sp^2-hybridized aromatic carbonaceous structures renders highly polar solvents devoid of amphiphilic properties as poor solvents for optimal dispersion. Consequently, CNTs dispersed in largely aqueous solutions typically stipulate the use of electrically insulating surfactants (*e.g.*, sodium dodecylbenzene sulfonate and poly-

[a] Institute for NanoEnergy, Department of Physics, University of Houston, Science and Research Building 1, Houston, Texas 77204, USA. E-mail: alexw6626@gmail.com
[b] Department of Electrical and Computer Engineering, University of Houston, Houston, Texas 77204, USA
†Electronic supplementary information (ESI) available. See DOI: 10.1039/c9nr00216b

ethylene glycol *p*-(1,1,3,3-tetramethylbutyl)-phenyl ether), which have been shown to adversely affect the electronic transport properties of the resulting bulk nanocomposite system.[23–25] Because CNT-filled polymeric nanocomposites typically suffer from poor bulk electrical conductivity, retaining the charge transport properties of the CNTs themselves is paramount towards materializing highly conductive disordered systems. While chemical functionalization and deagglomeration of CNTs is particularly useful for enhancing filler/host-polymer interfacial interactions, the acute oxidation and mechanical exfoliation (*e.g.*, ultrasonication) techniques often implemented are known to irreparably disrupt the desirable intrinsic electronic structure of the CNTs either *via* physical fragmentation or the introduction of electron scattering defect sites.[26,27]

In this work, surfactant-free aqueous *n*-methyl-2-pyrrolidinone (NMP)/dimethylformamide (DMF) solutions were implemented in the process of assembling multi-walled carbon nanotube (MWCNT)/polyurethane (PU) nanocomposites using a solvent-mixing method and minimal mechanical processing in an effort to preserve the desirable physical properties of the MWCNTs used while concomitantly yielding sufficiently homogeneous filler dispersions within the host matrix.[28,29] PU was selected in consideration of its ubiquitous use in diverse applications ranging from industrial and architectural coatings to state-of-the-art biomedical materials.[30,31] While PU-based host-matrices have been implemented in assembling MWCNT-filled nanocomposite materials, bulk electroconductivities remain comparatively low due largely to the implementation of concentrated oxidizing agents (*e.g.*, HNO_3, H_2SO_4, and $KMnO_4$) adopted in their respective oxidation procedures. Refer to Table 1. The present work evaluates the DC electronic transport properties of MWCNT/PU nanocomposites and how highly conductive disordered nanocomposite systems are realizable through the formation of percolating random networks of high-aspect ratio MWCNTs. Both pristine MWCNTs (P-MWCNTs) and mildly oxidized MWCNTs (O-MWCNTs) were evaluated as filler nanomaterials. Theoretical charge transport mechanisms across these random MWCNT networks are described *via* tunneling-assisted direct-charge transfer within the Landauer–Büttiker formalism.[32]

In application, nanocomposite devices are often subjected to inimical environmental conditions (*e.g.*, moisture/water, temperature fluctuations, electromagnetic (EM) irradiation, *etc.*) capable of compromising device performance. For instance, water in both the liquid and crystalline form collected in waveguides or on the surfaces of antennas has been shown to result in signal attenuations as high as 10 dB at a microwave frequency of 28 GHz,[39,40] which corresponds to a 90% attenuation of the incident EM wave at that frequency. While fluoropolymer-based composite materials exhibit excellent weathering properties, their roles are highly application specific and cost prohibitive, limiting their use in conventional applications. As such, scalable techniques for the surface modification of non-fluorinated structural polymers like PU to improve weatherability are of increasing importance. As a tertiary component of this work, assembled nanocomposite surfaces were functionalized *via* chemical vapor deposition (CVD) of the perfluoroalkylsilane (tridecafluoro-1,1,2,2-tetrahydrooctyl)trichlorosilane (TDFTS), which possesses three readily hydrolysable halogen moieties that facilitate chemisorption with the substrate and a highly non-polar linear perfluoroalkyl chain that imparts the substrate with exceptionally low surface energy properties. As a facile proof of concept to demonstrate the efficacy of this surface functionalization technique, the resistance across assembled nanocomposites both with and without hydrophobic surface modification were measured and recorded at set time intervals of immersion in de-ionized water.

The overarching objectives of the present work are: (1) the communication of a method by which scalable MWCNT-based polymer nanocomposites with exceptional charge transport properties are attained through percolating random networks of MWCNTs using nondestructive synthesis techniques and (2) demonstrate how surface functionalization of the resulting nanocomposite materials can effectively mitigate the detrimental effects of water ingress from environmental conditions that such materials are expected to perform under.
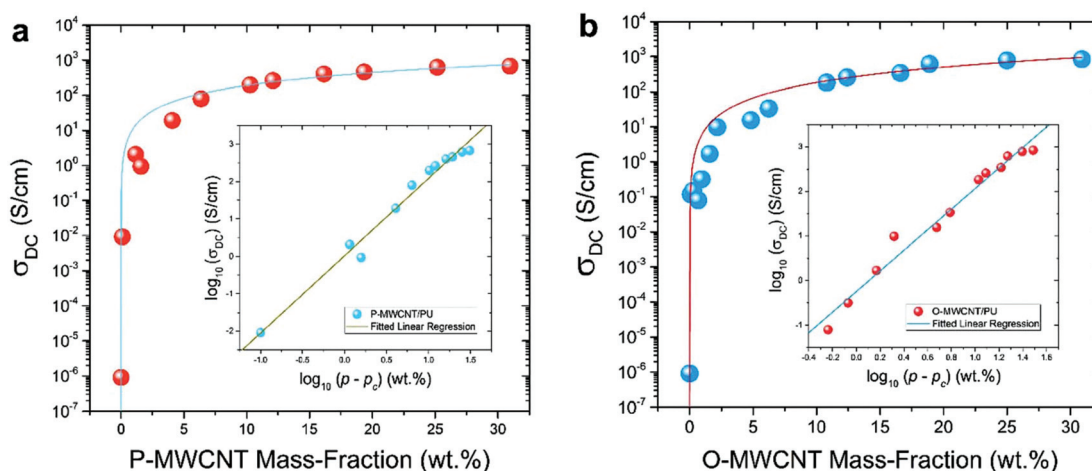
Results and discussion

DC electronic transport properties

The DC electrical conductivities of assembled composites measured *via* two-terminal sensing were plotted against the filler loading as shown in Fig. 1a and b. Resulting data points were fitted with a non-linear Belehradek-type power function modeled on the classical scaling law given by:

$$\sigma_{DC} = \sigma_o(p - p_c)^\tau, \quad p > p_c \tag{1}$$

where σ_{DC} is the DC conductivity of the bulk composite, σ_o is a parameter dependent on the intrinsic conductivity of the filler, p is the concentration of filler, p_c is the critical concentration of filler corresponding to the formation of a percolating conductive network, and τ is a dimensionless critical exponent denoting the dimensionality of the conductive network. It should be noted that σ_o can be expressed in terms of the

Table 1 A comparison between typical electrical conductivity values of MWCNT/PU nanocomposites at different MWCNT-loadings and the value obtained for a MWCNT/PU nanocomposite assembled in this work at a 10.3 wt% MWCNT-loading

DC Electrical conductivity (S cm^{-1})	Loading (wt%)	Ref.
7.3	2.5%	33
21.0	76.2%	34
9.0×10^{-3}	10%	35
1.0×10^{-3}	1.5%	36
7.4×10^{-1}	>2.5%	37
4.5×10^{-1}	7.0%	38
198.4 ± 2.8	10.3%	This work

Fig. 1 (a) A semi-log plot of the DC conductivity of the P-MWCNT/PU composites and (b) O-MWCNT/PU composites prepared in this work as a function of filler mass-fraction measured *via* two-terminal sensing; the insets are corresponding log−log plots of the DC conductivity as a function of the difference between the filler mass-fractions and percolation thresholds.

intrinsic conductivity σ_f and aspect ratio γ of the filler as follows:[41]

$$\sigma_o = \sigma_f \times 10^{0.85[\log(\gamma)-1]}. \tag{2}$$

Percolation threshold values were calculated by determining the optimal concentration of filler yielding the best least-squares linear regression to log–log plots of the DC conductivity of assembled nanocomposites as a function of the difference between p and p_c using a Levenberg–Marquardt iteration algorithm. P-MWCNT/PU and O-MWCNT/PU nanocomposites assembled in this work exhibited percolative behavior at low critical concentrations of $p_{c_{pristine}}$ = 0.001 wt% and $p_{c_{oxidized}}$ = 0.093 wt%, respectively. Corresponding critical values of dimensionality of $\tau_{pristine}$ = 2.067 ± 0.094 and $\tau_{oxidized}$ = 2.304 ± 0.114 were calculated for P-MWCNT/PU and O-MWCNT/PU composites, respectively, strongly supporting the existence of three-dimensional (3D) percolating conductive networks permeating the PU host matrix. In randomly distributed CNT-filled polymeric nanocomposite systems, 3D percolating networks typically correspond to empirical critical exponent of dimensionality values ranging between 1.3 and 3.1.[42,43] Saturated DC conductivity values as high as 674 ± 10 S cm^{-1} for P-MWCNT/PU composites and 839 ± 72 S cm^{-1} for O-MWCNT/PU composites at a filler loading of 30.9 wt% were measured as presented in Fig. 1. The comparatively low percolation threshold values calculated and exceptionally high electroconductivity values measured for assembled nanocomposites may in part be attributed to the minimal mechanical processing procedures adopted in this work, which effectively preserved the structural integrity and high aspect ratios of the MWCNTs used. Additionally, the use of amide-functional solvents like DMF have been shown to favor the formation of smaller CNT bundles with a narrower bundle size distribution,[44,45] resulting in a more homogeneous interpenetrating conductive network throughout the PU host matrix.

It should be noted that higher filler dispersions facilitated through chemical functionalization or mechanical dispersion do not necessarily imply lower percolation thresholds and higher conductivities. Chemical functionalization disrupts the delocalization of π-electrons on the conjugated surfaces of CNTs, resulting in the formation of localized electron scattering centers that adversely affect the intrinsic conductance of such materials. In congruence, the O-MWCNTs used in this work to assemble O-MWCNT/PU nanocomposites likely yielded higher filler dispersions promoted by the presence of polar oxygen-containing moieties; however, the higher percolation threshold value calculated for O-MWCNT/PU composites indicate increased inter-filler proximity, requiring higher-filler loadings to establish an interconnected conductive network. Higher dispersions at lower filler mass fractions have been shown to result in localized regions of mildly agglomerated CNTs engulfed by insulating dielectric host polymer,[46] corresponding to localized energy states separated by tunneling energy barriers. In disordered systems like conductive filler-loaded nanocomposites, electronic transport through the bulk matrix below the percolation threshold occurs primarily through either incoherent electron hopping or coherent electron tunneling as opposed to direct charge transfer. Ergo, decreasing the inter-filler proximity decreases the potential energy barrier between adjacent hopping or tunneling sites. This corresponds to an increased probability for successful electron tunneling or hopping, and as a corollary, an increased electron tunneling or hopping rate.[47,48]

Micro-/nano-structural analysis *via* field emission-scanning electron microscopy

Representative of all nanocomposites assembled in this work, the general microstructure and morphology of assembled 10.8 wt% O-MWCNT/PU nanocomposite surfaces consists of interconnected nodes and pore spaces, as illus-
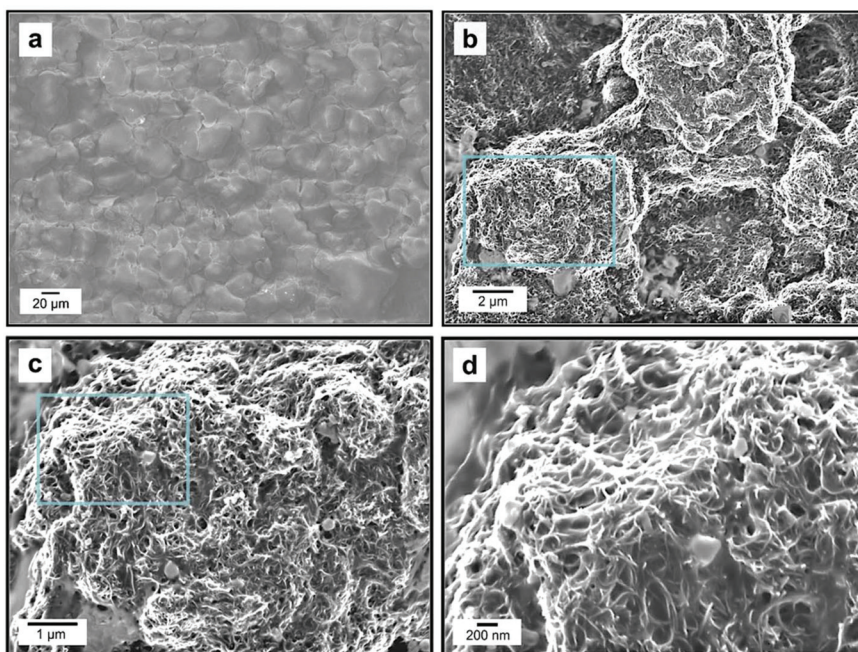
Fig. 2 (a) Large-scale micrograph illustrating the botryoidal surface morphology of a 10.8 wt% O-MWCNT/PU nanocomposite comprised of densely-packed interlocking nodules. (b) A higher magnification micrograph of the area demarcated in blue in (b), revealing the surface morphology of the densely-packed clusters as being comprised of a dense random network of MWCNTs embedded in a PU matrix. (c) A higher magnification micrograph of the area demarcated in blue in (b), where individual MWCNTs are resolved. (d) Upon further magnification of (c), a complex, random, percolating network of intersecting high-aspect ratio MWCNTs embedded in a PU matrix is observed.

trated in Fig. 2a. These nodes and linkages are comprised of densely packed O-MWCNT/PU clusters as revealed by a higher magnification micrograph presented in Fig. 2b. Upon further magnification, the nanostructure of these interconnected nodes is resolved as a uniformly distributed random network of high aspect ratio O-MWCNTs intimately embedded in a PU matrix, as shown in Fig. 2c. Structurally, the system of interconnected nodes is a result of bridging between the initial crosslinked PU microbeads (mean diameter of 4.9 μm) used to prepare the O-MWCNT/PU nanocomposites. From Fig. 2d, it is evident that electrical conduction through the bulk composite at higher filler-loadings above the percolation threshold occurs largely *via* direct inter-nanotube charge transfer facilitated through percolating conductive pathways established *via* permeating random O-MWCNT networks. For all FE-SEM micrographs obtained of P-MWCNT/PU and O-MWCNT/PU nanocomposite samples above their respective percolation threshold, no evidence of inhomogeneous filler aggregation/isolated electron trap sites was observed.

Charge transport mechanisms above percolation

Charge carrier mobility in conductive disordered systems is a derivative of the microstructure of each respective system. While the precise interplay between microstructure, electronic transport properties, and corresponding mechanisms-of-action are still poorly understood, recent studies[49,50] have demonstrated the critical dependency of charge transport

on the degree of paracrystallinity in disordered/amorphous materials. Higher degrees of structural disorder amount to proportionally larger energy level variations across the bulk material, resulting in deeper charge carrier trap sites, requiring larger activation energies. In contrast, electron transport mechanisms governing effective charge transfer across the bulk nanocomposites assembled in this work ($\forall p \geq p_c$) can be described within the frameworks of tunneling-enhanced direct charge transfer. As opposed to isolated energy states separated by large tunneling barriers, as schematically illustrated by the shaded purple circles in Fig. 3a and b, there exists a micro/nanoscopic random network of densely interconnected conductive pathways, as illustrated by the shaded light-blue circles in Fig. 3c and d, where interconnected herein implies mean inter-CNT separation distances at or below the nanoscale. A schematic illustration of the different electron transport mechanisms across the system is provided in Fig. 3e. At the mesoscopic scale, the dimensions of such inter-nanotube contact regions have been shown to approach that of the corresponding Fermi wavelength λ_{Fermi}, (*i.e.*, the de Broglie wavelength of Fermi level electrons) and momentum relaxation length ℓ_M (*i.e.*, the average distance traversed by electrons between collisions with scattering centers (*e.g.*, impurities/defects).[51,52] Such small tunneling distances, on the order of the van der Waals separation distance $d_V = 3.4$ Å, are conducive to ballistic transport across small tunneling energy barriers.[53,54] From the Landauer–Büttiker formalism, the *I–V* character-
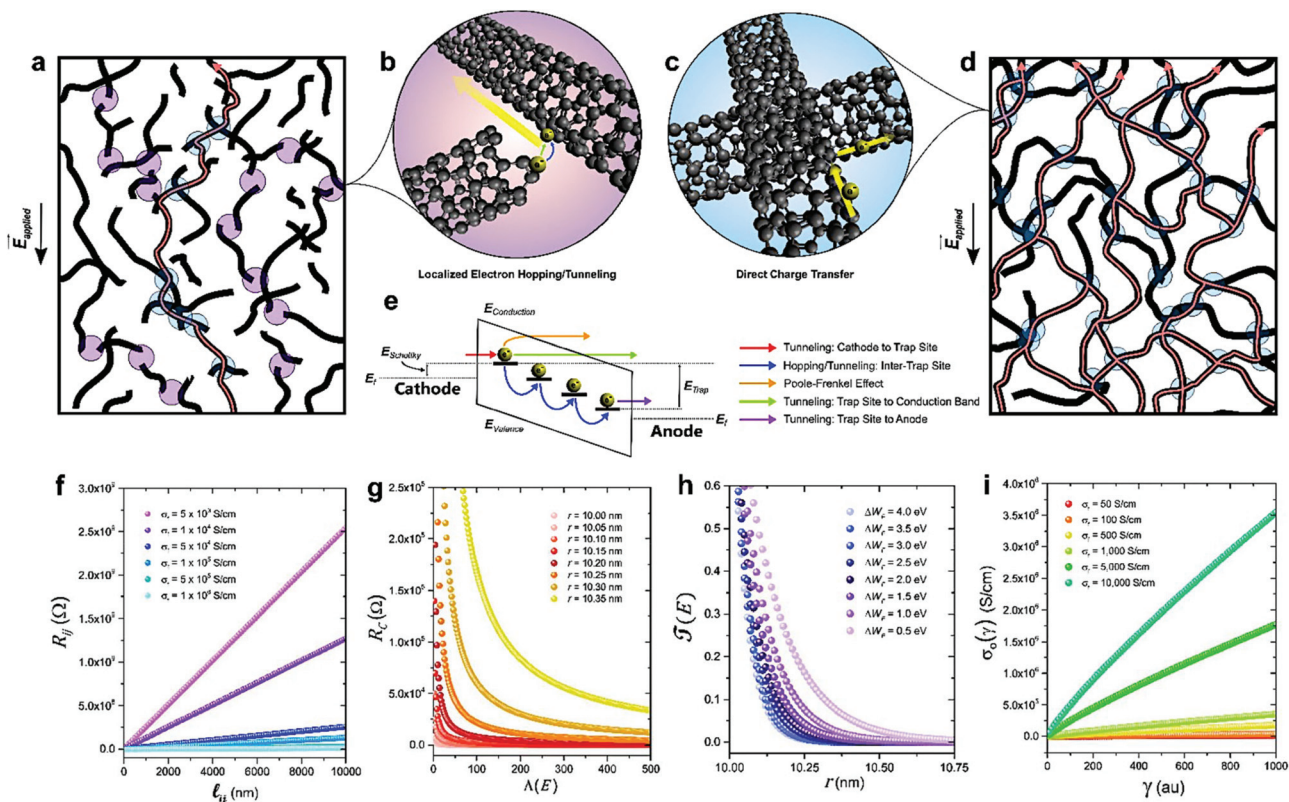
Fig. 3 (a) Schematic illustration of electron transport across a nanocomposite implementing damaged, low-aspect ratio CNTs. Here, the purple and blue shaded circular overlays represent regions of inter-nanotube charge transfer *via* low-probability localized electron hopping/tunneling between isolated conductive domains and high-probability direct charge transfer across a small ballistic tunneling junctions of contact resistance R_C, respectively. The faint red arrows represent percolating pathways of interconnected CNTs. (b) Schematic illustration of low-probability electron hopping/tunneling sites (purple shaded circles) between localized energy states separated by large potential barriers, resulting in disconnected trap sites and correspondingly low nanocomposite conductivity. (c) Schematic illustration of ballistic tunneling sites (blue shaded circles) facilitating inter-nanotube direct charge transfer. (d) Schematic illustration of electron transport across a nanocomposite implementing undamaged, high-aspect ratio MWCNTs. (e) Schematic illustration of the possible electron transport mechanisms across a nanocomposite, where the colored arrows are defined in the adjacent legend. Here E_f, $E_{Schottky}$, $E_{Valence}$, $E_{Conduction}$, and E_{Trap} denote the Fermi energy level, Schottky barrier height, valence band energy, conduction band energy, and inter-trap site potential barrier, respectively. (f) Intrinsic CNT resistance between nodes i and j as a function of CNT length between nodes i and j for varying intrinsic conductivity values. (g) Contact resistance as a function of the number of conduction channels for different inter-axial separation distances between neighboring CNTs. (h) Tunneling probability as a function inter-axial separation distance between neighboring CNTs for varying tunneling barrier heights. (i) Conductivity constant plotted as a function of CNT aspect ratio for different intrinsic conductivity values.

istics across such ballistic transport tunneling junctions is given by

$$I_t = \frac{e}{\pi \hbar} \int_0^\infty \mathcal{T}(E) \Lambda(E) \left[\frac{1}{(e^\psi + 1)} - \frac{1}{(e^\varphi + 1)} \right] dE, \quad (3)$$

$$\psi = \frac{E_e - \xi - eV_{bias}}{k_B T}, \quad (4)$$

$$\varphi = \frac{E_e - \xi}{k_B T}, \quad (5)$$

where I_t is the tunneling current, e is the elementary charge, $\hbar$ is the reduced-Planck's constant ($\hbar = h/2\pi$), $\mathcal{T}(E)$ is the transmission probability for an electron to tunnel across the potential energy barrier (ΔW_F), $\Lambda(E)$ is the net number of conduction channels/junctions representative of the number of energy bands contributing towards conductance, E_e is the electron

energy level, ξ is the chemical potential of the CNT, V_{bias} is the bias voltage across the tunneling barrier, k_B is the Boltzmann constant, and T is the CNT temperature. It should be noted that eqn (3) accounts for spin degeneracy. An expression for the transmission probability $\mathcal{T}(E)$ is obtained using the Wentzel–Kramers–Brillouin (WKB) approximation method as follows:

$$T = \begin{cases} \exp(-d_V \chi), & 0 < r \le D_{outer} + d_V \\ \exp[-\chi(r - D_{outer})], & D_{outer} + d_V < r \le D_{outer} + d_{cutoff} \end{cases}, \quad (6)$$

$$\chi = \frac{\sqrt{8 m_e \Delta W_F}}{\hbar}, \quad (7)$$

where m_e is the mass of an electron, ΔW_F is the potential barrier height given by the difference between the work func-

tions of the CNT and dielectric polymer, r is the distance between the longitudinal nanotube axes of two neighboring CNTs, D_{outer} is the outer CNT diameter, d_{V} is the van der Waals separation distance (here, $d_{\text{V}} = 0.34$ nm),[53] and d_{cutoff} is the threshold distance within which tunnelling effects much be considered.[55,56] Exploiting its asymptotic behavior, a Sommerfeld expansion of eqn (3) with respect to temperature provides a facile means by which to holistically represent the large number of tunneling junctions without considering the exact configurations and chiralities of the individual nanotubes comprising such junctions.[57] In doing so, eqn (3) becomes

$$I_{\text{t}} = \frac{e}{\pi\hbar} \left\{ \int_{\xi}^{\xi+eV_{\text{bias}}} \Theta(E)\text{d}E + \frac{(\pi k_{\text{B}}T)^2}{6}\left[\frac{\text{d}(\Theta(E))}{\text{d}E}\right]\Bigg|_{\xi}^{\xi+eV_{\text{bias}}} + \mathcal{O}\left(\frac{k_{\text{B}}T}{\xi}\right)^4 \right\},$$
(8)

$$\Theta(E) = T(E)\Lambda(E),$$
(9)

where $\mathcal{O}\left(\dfrac{k_{\text{B}}T}{\xi}\right)^4$ denotes additional expansion terms that are a multiplicative factor of $\left(\dfrac{k_{\text{B}}T}{\xi}\right)^n \forall n \geq 4$. Reducing terms in eqn (8) for low bias voltages[58] and applying Ohm's law yields an expression for the contact resistance R_{C} between two CNTs separated by an inter-axial distance $d_{\text{V}} \leq r \leq d_{\text{cutoff}}$, where $d_{\text{cutoff}} \approx 2\lambda_{\text{Fermi}}$ is the critical separation distance beyond which tunneling effects are neglected:

$$R_{\text{C}} = \frac{V_{\text{bias}}}{I_{\text{t}}}$$
$$= \frac{\pi\hbar}{e^2}\left[\mathcal{T}\Lambda\left(1 + \frac{1}{6}\left(\frac{\pi k_{\text{B}}T}{\Delta W_{\text{F}}}\right)^2 \ln(\mathcal{T})(\ln(\mathcal{T})+1)\right)\right]^{-1}.$$
(10)

However, since $k_{\text{B}}T \ll \Delta W_{\text{F}}$, the temperature-dependent terms in eqn (10) can be effectively ignored for sufficiently small T (~300 K) such that

$$R_{\text{C}} = \frac{\pi\hbar}{e^2}\left(\frac{1}{\mathcal{T}\Lambda}\right).$$
(11)

A schematic illustration for such a direct charge transfer mechanism is presented in Fig. 3a and d, where the light-blue shaded circles overlaid atop intersecting MWCNTs represent ballistic transport junctions of contact resistance R_{C} given by eqn (11). Note from Fig. 3f, that the intrinsic resistance R_{ij} between nodes i and j linearly increases with the separation distance ℓ_{ij} between nodes i and j, where R_{ij} is given by the Drude model[57] as follows,

$$R_{ij} = \frac{4\ell_{ij}}{\pi\sigma_{\text{f}}D_{\text{outer}}^2}.$$
(12)

R_{ij} curves were plotted for 6 different σ_{f} values ranging from 5000 S cm^{-1}–10^6 S cm^{-1}, which are typical empirical values for the intrinsic conductivity of MWCNTs across a range of chiralities and geometries.[59] In Fig. 3f, the outer nanotube diameter is taken as $D_{\text{outer}} = 10$ nm, which is the approximate outer diameter of the MWCNTs used in this work. As illustrated in

Fig. 3g, R_{C} decreases asymptotically as Λ increases, where small changes in r correspond to large changes in R_{C}. Recent experimentally corroborated numerical models[59,60] have demonstrated the importance of the value of Λ in realizing high-conductivity nanocomposites, where increasing Λ corresponds to a proportional increase in bulk conductivity resulting from a decrease in R_{C}. In comparison to metallic single-wall CNTs (SWCNTs), which exhibit two Fermi level-crossing energy bands ($\Lambda = 2$),[61] MWCNTs have been shown to exhibit exceptionally large Λ values ranging between 400–500.[62] This follows as a result of additional energy band contributions from the outermost contiguous walls capable of extending to the Fermi level. Fig. 3h illustrates the critical dependency for successful electron tunnelling on r, where the dependency of $\mathcal{T}(E)$ on the tunnelling barrier height (ranging here from 0.5–4.0 eV) is also presented. Note that $\mathcal{T}(E)$ exponentially decreases in correspondence to a comparatively small increase in r on the order of λ_{Fermi}. To further illustrate the dependency of the conductivity parameter on the aspect ratio γ, eqn (2) was plotted using intrinsic conductivity values ranging from 50–10 000 S cm^{-1}, as illustrated in Fig. 3i. From Fig. 3i, it is apparent that the aspect ratios of nanotubes of higher intrinsic conductivity must be preserved to optimize the conductivity of the resulting composite system.

FTIR-ATR, UV-Vis-NIR, and Raman spectroscopy

The prominent absorption bands of CNTs across the UV-Vis spectrum are uniquely characteristic of the EM excitation of individually dispersed nanotubes corresponding to 1D van Hove singularities (i.e., agglomerates or bundles of CNTs do not produce the same characteristic absorption bands).[63] Consequently, UV-Vis spectroscopy affords a facile way by which to characterize the electronic structure and degree of dispersion of MWCNTs. UV-Vis absorbance spectra of both the pristine and mildly oxidized MWCNTs used in this work were evaluated as presented in Fig. 4a. Apart from the chemical functionalization/oxidation procedure implemented in producing the O-MWCNTs, both samples were treated identically. The strong absorbance peak at 275 nm (4.51 eV) is assigned to the $\pi \rightarrow \pi^*$ interband electronic transition, which occurs at the M point of the Brillouin zone where the imaginary component of the permittivity $\varepsilon_\perp$ perpendicular to the nanotube axis is a maximum.[64] This electronic transition, referred to as π-plasmon resonance, is representative of the collective oscillations of π-electrons on the exohedral nanotube surfaces. As illustrated in Fig. 4a, O-MWCNTs exhibited stronger absorbance across the UV-Vis spectrum likely as a result of higher dispersions, which is in agreement with the larger percolation threshold value calculated for the O-MWCNT/PU nanocomposites assembled in this work. The higher dispersions evidenced in UV-Vis spectra for O-MWCNTs may also account for the higher saturated conductivities measured for assembled O-MWCNT/PU composites as compared to their P-MWCNT/PU counterparts, corresponding to a higher more uniform conductive network density throughout the bulk of the host matrix.
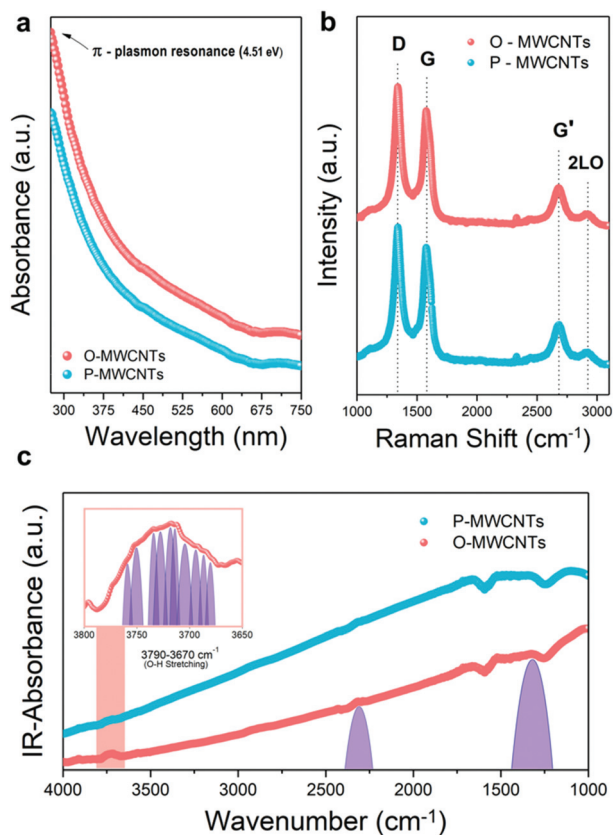
Fig. 4 (a) UV-Vis spectra of the P-MWCNTs (blue) and O-MWCNTs (red) used in this work. (b) Raman spectra of the P-MWCNTs (blue) and O-MWCNTs (red) used in this work. (c) IR-absorbance spectra of the P-MWCNTs (blue) and O-MWCNTs (red) used in this work. The inset and shaded peaks denote signature peaks corresponding to O−H stretching.

This is further supported by Raman spectra of the P- and O-MWCNTs used in this work. As presented in Fig. 4b, four characteristic bands of MWCNTs at 1340 cm^{-1} (D-band), 1580 cm^{-1} (G-band), 2680 cm^{-1} (G′-band), and 2925 cm^{-1} (2LO-band) are readily observable. The prominent G-band results from one-phonon scattering off the zone-centered E$_{2g}$-symmetric first-order phonon mode of in-plane C=C bonds in sp^2-hybridized graphitic networks.[65] Contrasting second-order Raman scattering processes due to one-phonon double reso-nance and two-phonon double resonance resulting from defect sites and/or sp^3-hybridized amorphous carbon give rise to the D- and G′-bands, respectively, where the G′-band exists as an overtone mode of the D-band.[65,66] The 2LO-band results from a two-phonon double resonance scattering process and is an overtone of the LO mode attributed to intervalley scattering. The ratio $\alpha = I_D/I_G$ of the intensity of the D-band over the inten-sity of the G-band is used as a facile means by which to ident-ify variations/changes in the physicochemical properties of CNTs. Comparing the Raman intensity maxima of the D- and G-bands for P- and O-MWCNTs, respectively, yielded $\alpha_{pristine}$ = 1.17 and $\alpha_{oxidized}$ = 1.21. The slight increase in α in the Raman spectra of O-MWCNTs is attributed to the introduction of oxygen-containing functional groups (principally – OH groups)

resulting from mild oxidation in H$_2$O$_2$.[67] Because $\alpha_{oxidized}$ corresponds to a mere 3.42% increase as compared to $\alpha_{pristine}$, it can be reasoned that no significant structural damage resulted from the mild oxidation processes implemented in this work.

Thermogravimetric, differential calorimetric, and differential thermal analysis

Thermogravimetric, differential calorimetric, and differential thermal analyses were conducted to characterize the thermal stability of assembled O-MWCNT/PU nanocomposites with respect to neat PU. TGA thermograms of neat PU and 0.0932 wt% O-MWCNT/PU samples are presented in Fig. 5a, where the thermal decomposition of both can be partitioned into two distinct stages. The first stage of decomposition, corresponding to an ~9% mass loss, occurs between 135–250 °C and is attributed to a combination of two events: (1.) removal of water adsorbed via hydrogen bonding and (2.) initial decomposition of urethane linkages, which have a lower bond energy than urea linkages.[68] The second stage of decomposition occurring between 250–375 °C is attributed to the thermal degradation of urea linkages and polyol moieties. It should be noted that the second decomposition stage can be further divided into two contiguous segments comprised of an exothermic event between 250–290 °C and an endothermic event between 290–375 °C, as evidenced in the DSC thermo-
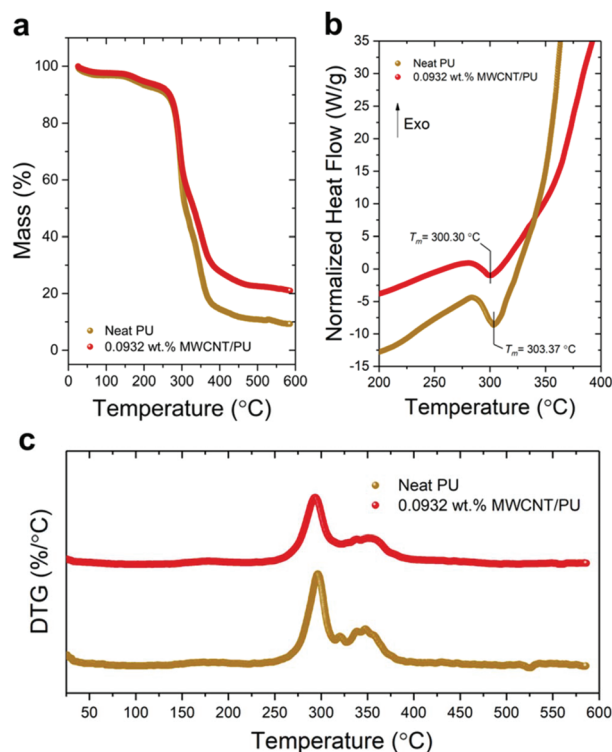
Fig. 5 (a) TGA thermograms of neat PU and 0.0932 wt% MWCNT/PU samples. (b) Weight-corrected heat flow curves of neat PU and 0.0932 wt% MWCNT/PU samples. (c) Differential thermogravimetric curves of neat PU and 0.0932 wt% MWCNT/PU samples.

gram presented in Fig. 5b. Here, 0.0932 wt% O-MCWNT/PU composite samples exhibit a slight down-shift in endothermic peak from 303 °C (neat PU) to 300 °C.

This endothermic peak shift is expected, as the thermal conductivity of the O-MWCNTs accelerates the rate at which principal energy carriers such as phonons transfer thermal energy to the bulk dielectric matrix.[69] Beyond the second decomposition stage, steady pyrolysis of the bulk material is observed. Upon completion of the linear heating cycle to 600 °C, neat PU and 0.0932 wt% O-MWCNT/PU samples exhibit a 90.72% and 78.98% mass loss, respectively. This demonstrates that the addition of well-dispersed O-MWCNTs at mass-fractions as small as 0.0932 wt% yields significant improvement (13.84%) in thermal stability, particularly during the endothermic event between 290–375 °C. In addition to physical and/or covalent interactions between O-MWCNTs and the PU host matrix, this enhancement in thermal stability may in part be due to the gas sequestration properties of MWCNTs, which could potentially trap volatile organics evolved during pyrolysis. Increased thermal stability is further corroborated by the differential thermogravimetric (DTG) curves presented in Fig. 5c. Maximum decomposition rates of 1.71% per °C and 1.25% per °C for neat PU and 0.0932 wt% O-MWCNT/PU

samples, respectively, occur at 297 °C and 293 °C. As compared to neat PU, less pronounced DTG peaks (smaller maxima) between 315–375 °C in the DTG curve for 0.0932 wt% O-MWCNT/PU provide further support for a thermal stabilization effect.

Sessile contact angle measurements and FTIR-ATR analysis

Markedly lower surface energies were obtained as a direct result of the physicochemical surface modification of O-MWCNT/PU nanocomposites via chemical vapor deposition of TDFTS, as schematically illustrated in Fig. 6a. From Fig. 6c, O-MWCNT/PU nanocomposites treated with TDFTS vapor exhibited sessile contact angles as high as $\theta_{treated} = 154°$, indicating the presence of a superhydrophobic surface; surfaces with contact angles $150° \leq \theta < 180°$ are classified as superhydrophobic. In comparison, otherwise identical untreated O-MWCNT/PU composite surfaces exhibited sessile contact angles as high as $\theta_{untreated} = 54°$. Refer to Fig. 6b. The transition to a superhydrophobic state may be attributed to the orientation of the perfluoroalkyl moieties in conjunction with the porous surface morphology of the O-MWCNT/PU composite surfaces. The fluoroalkyl chains of TDFTS are known to form helical arrangements[70] with a sufficient number of
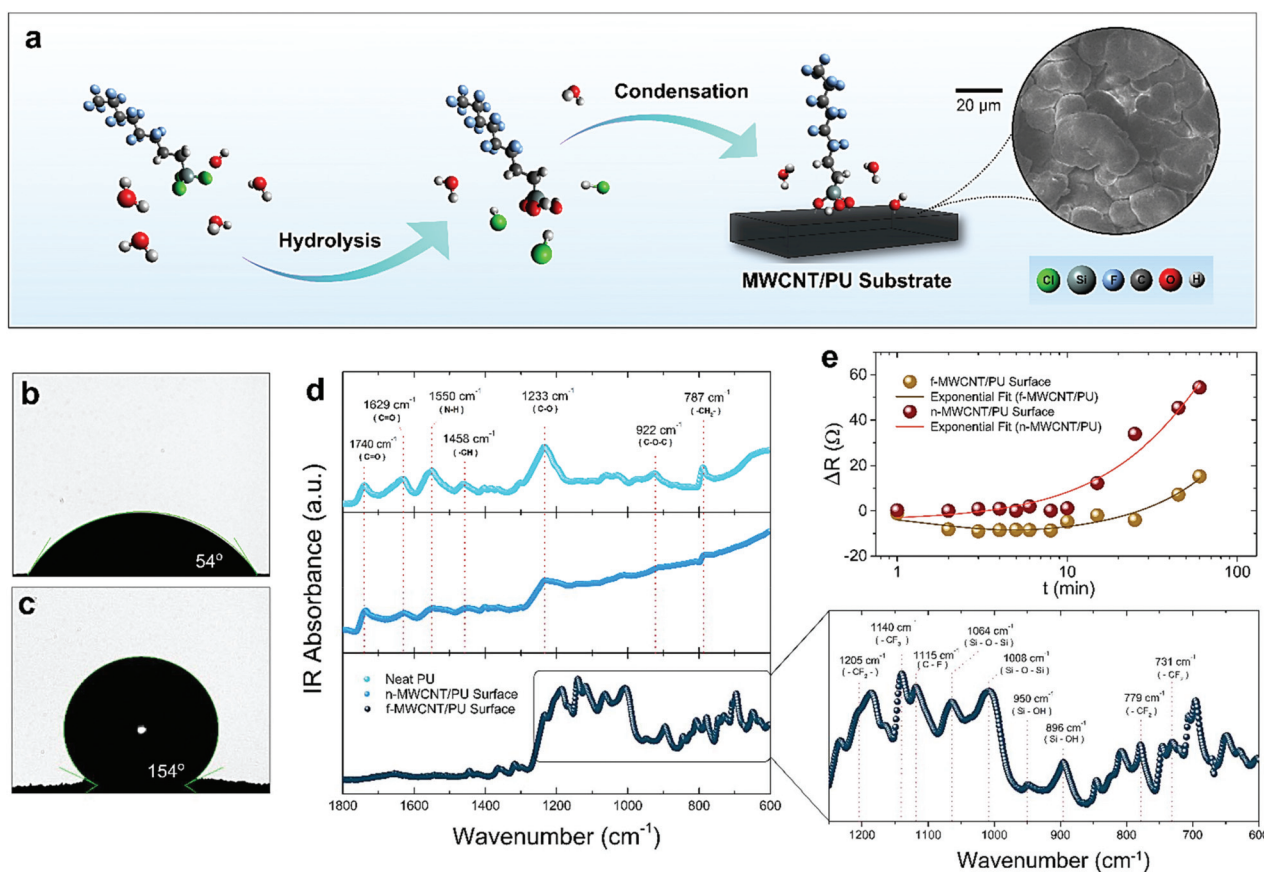
Fig. 6 (a) Generalized illustration of a possible reaction mechanism by which TDFTS may covalently anchor to a MWCNT/PU substrate. (b) Sessile contact angle measurement of 54° for a pristine MWCNT/PU composite surface. (c) Sessile contact angle measurement of 154° for a f-MWCNT/PU composite surface. (d) FTIR spectra of neat PU (top), pristine MWCNT/PU composite surface (middle), and f-MWCNT/PU composite surface (bottom). (e) Change in resistance (ΔR) plotted against immersion time.

degrees of freedom to accommodate an appreciable radius of gyration about the covalent anchoring sites through which the Si head is bonded. This effect works to mitigate any potential loss in decrease in surface energy due to low concentrations of TDFTS chemisorbed onto the O-MWCNT/PU substrate by increasing the effective surface coverage per TDFTS molecule. Because longer-chain alkyl organosilanes are more conducive to the formation of more ordered and compact self-assembling monolayers,[71,72] it can be reasoned that even lower surface energies can be achieved using longer perfluoroalkyl silanes like (heptadecafluoro-1,1,2,2-tetrahydrodecyl)trichlorosilane in place of TDFTS under otherwise identical conditions.

The physisorption and/or chemisorption of TDFTS onto MWCNT/PU composite surfaces was studied using FTIR-ATR spectra of neat PU, pristine MWCNT/PU (n-MWCNT/PU), and TDFTS-functionalized MWCNT/PU (f-MWCNT/PU) surfaces. Strong absorbance bands at 1740 cm^{-1} (C=O stretching),[73,74] 1629 cm^{-1} (C=O stretching),[73] 1550 cm^{-1} (N–H bending),[73] 1458 cm^{-1} (C–H bending),[75] 1233 cm^{-1} (C–O stretching),[75] 922 cm^{-1} (C–O–C valence vibrations (C–O stretching)),[76] and 787 cm^{-1} (=C–H bending and ring puckering)[77] are observed in FTIR spectra of both neat PU and n-MWCNT/PU nanocomposite surfaces. Increased absorbance across the far-mid IR in FTIR spectra of n-MWCNT/PU surfaces is attributed to the broadband IR absorbance of MWCNTs. In contrast, FTIR spectra of f-MWCNT/PU surfaces revealed multiple new IR absorbance peaks between 600–1300 cm^{-1} as presented in Fig. 6d.

Characteristic IR absorbance bands at 1205 cm^{-1} (CF$_2$ stretching),[78] 1140 cm^{-1} (CF$_3$ stretching), 1115 cm^{-1} (C–F stretching),[79] 1064 cm^{-1} (CF$_3$ symmetric stretching; Si–O–Si stretching),[80,81] 1008 cm^{-1} (Si–O–Si stretching),[81,82] 950 cm^{-1} (Si–OH symmetric stretching),[83] 896 cm^{-1} (symmetric stretching),[83] 779 cm^{-1} (CF$_2$ scissoring),[80] and 731 cm^{-1} (CF$_2$ symmetric stretching)[80] strongly support the presence of TDFTS either adsorbed or absorbed onto the MWCNT/PU surface. Siloxane stretching modes at 1008 cm^{-1} and 1064 cm^{-1} indicate covalent crosslinking between adjacent TDFTS molecules condensed on the surfaces of f-MWCNT/PU samples, effectively forming a covalently interconnected low surface energy layer. Because the penetration depth of the evanescent field resulting from incident IR radiation in ATR-mode is on the order of 1–2 μm for a ZnSe internal reflection element, characteristic vibrational modes present in the FTIR spectra of neat PU and n-MWCNT/PU surfaces are masked by the strong vibrational responses from TDFTS moieties.

Effects of surface hydrophobization on electronic transport

As a facile proof of concept, the resistance across pristine and hydrophobically modified MWCNT/PU composites was measured periodically while immersed in de-ionized water. After 1 h of immersion, it was found that the increase in electrical resistance across a pristine MWCNT/PU composite was greater than that across a hydrophobically modified one by a factor of 3.56. Refer to Fig. 6e. This effect may be attributed to the gradual swelling of the bulk PU matrix through the absorp-

tion of water and subsequent hydrolysis of polyester-based polyol components following prolonged immersion.[84] Consequently, at swelling sites, a redistribution/reorientation of MWCNTs resulted in the localized breakdown of conductive networks, corresponding to the observed increase in bulk resistance, which followed a non-linear exponential curve. Increasing the internanotube distance effectively decreases the electron tunneling probability through tunneling junctions between MWCNTs. Such a swelling effect in composite matrices is well-documented in the literature,[85,86] where the resulting change in resistance ΔR in response to matrix swelling can be expressed as

$$\Delta R = R_{\mathrm{o}}\left[\left(\frac{r}{r_{\mathrm{o}}}\right)\exp[\beta(r - r_{\mathrm{o}})] - 1\right], \qquad (13)$$

$$\Delta R = R - R_{\mathrm{o}}, \qquad (14)$$

where R is the final resistance, R_{o} is the initial resistance, r is the final inter-filler distance, r_{o} is the initial inter-filler distance, and β is an empirically determined parameter dependent on the height of the potential energy barrier E_{nm} between adjacent filler particles n and m and is given by

$$\beta = (25.57 \times 10^{18})\sqrt{E_{nm}}. \qquad (15)$$

Hydrophobically modified MWCNT/PU nanocomposites exhibited a slight decrease in resistance followed by the onset of a gradual increase in resistance after ~45 min of immersion. In contrast to pristine MWCNT/PU composites, the hydrophobically modified MWCNT/PU composites assembled in this work exhibited a delayed onset of resistance increase, which is attributed to the presence of highly non-polar perfluoroalkyl moieties decorating the effective surface area of treated composites, as illustrated in Fig. 6a. The observed increase in ΔR in hydrophobically modified MWCNT/PU composites after 45 min is believed to arise from slow seepage of water through the composite edges at the interface between the composite and the ITO substrate that may not have received adequate contact with TDFTS vapor during the treatment process. Notwithstanding the eventual increase in ΔR, the 7.2 Ω and 15.3 Ω increase in ΔR after 45 min and 60 min of immersion corresponds to a 533% and 256% decrease in ΔR, respectively, as compared to otherwise identical untreated MWCNT/PU nanocomposites subjected to identical testing conditions.

Experimental section

Materials

Purified MWCNTs (≥98% carbon basis) with outer diameters of 10 nm ± 1 nm, inner diameters of 4.5 nm ± 0.5 nm, and lengths (along the nanotube axis) of 3–6 μm were obtained from Sigma Aldrich but synthesized by SouthWest NanoTechnologies Inc. Said MWCNTs were synthesized *via* catalytic CVD, yielding nanotubes 6–8 walls thick with aspect ratios between 350–500. Cross-linked PU micro-spheres of mean diameter 4.9 μm in powdered form were obtained from

Supercolori S.P.A under the trademark name Decosphaera Transp. T. Hydrogen peroxide (H_2O_2) (30% (v/v)) (aq.) was obtained from Macron Fine Chemicals. De-ionized water (DI-H_2O) (Fluka Analytical), n-methyl-2-pyrrolidinone (NMP), (≥99.5%), dimethylformamide (DMF) (99.8%), polyethyleneimine (branched, $\bar{M}_w$ = 25 000) (PEI), (tridecafluoro-1,1,2,2-tetrahydrooctyl)trichlorosilane (TDFTS) (98%), and indium tin oxide (ITO)-coated poly(ethyleneterephthalate) (PET) (8–12 Ω sq^{-1}, ITO thickness = 120–160 nm) were sourced from Sigma Aldrich. All materials were used as received from the vendor unless specified otherwise.

Oxidation of MWCNTs

2.06 g of pristine MWCNTs was dispersed in 150 mL of a solvent blend of DMF and NMP, prepared to a volumetric ratio of 2 : 1 (DMF : NMP), in a 250 mL round-bottom flask. Additionally, 80 mL of H_2O_2 (30% (v/v)) was added as an oxidizing reagent. The MWCNT/NMP/DMF mixture was vigorously stirred for 10 min. The resulting mixture was briefly sonicated for 2 min. A uniform, viscous, sludge-like mixture was obtained. Following sonication, the mixture was magnetically stirred at room temperature (17–21 °C) for 7 days. After 7 days of stirring, the resulting mixture was centrifuged at 10 000 rpm for 30 min. This process was repeated once more with water and twice more with methanol. The washed oxidized MWCNTs (O-MWCNTs) were then dried at 40 °C for 48 h in a ventilated oven followed by an additional 2 h at 100 °C under a partial vacuum. The resulting solid was then milled using a glass stir rod to obtain a fine black powder.

Nanocomposite assembly

To characterize the DC electronic properties of the MWCNT/PU composites prepared in this work as a function of filler mass-fraction, thirteen different filler-loadings were prepared in accordance with the synthesis procedure described below. MWCNT/PU dry mixtures were transferred to thoroughly cleaned 2-dram glass vials. Refer to Tables S1 and S2 (ESI†). The dry MWCNT/PU mixtures were mixed by lightly tapping the glass vials against a solid surface until uniform mixtures were visually observed. 250 µL of NMP, 250 µL of DMF, and 1.5 mL of DI-H_2O were added to each vial, resulting in a 6 : 1 : 1 (water (vol.):NMP (vol.):DMF (vol.) aqueous NMP/DMF mixture. Additionally, 100 µL of an aqueous 1% (wt/v) PEI solution was added to each mixture to serve as a plasticizer. Subsequently, all mixtures were briefly sonicated for 5 min at 20 °C. All mixtures were then vigorously stirred for 20 min. After stirring, uniform mixtures were obtained which exhibited no signs of phase separation even after 2 h. However, all composite samples that were dropcast onto a characterization device were done so immediately following stirring to promote homogeneity. Once dropcast, nanocomposite samples were carefully transferred to a ventilated oven to dry/cure for 1 h at 70 °C.

DC electronic transport properties

A high-vacuum modular thermal evaporation system (Pfeiffer HiCube) with a turbo pump (Pfeiffer HiPace 80) was implemented in fabricating thin-film Au electrodes for use in characterizing the electronic transport properties of assembled nanocomposite materials. The dimensionality of the evaporated thin-film electrodes was characterized using a Tencor Alpha-Step 200 profilometer. To determine the DC conductivity of the MWCNT/PU nanocomposites, ~15 µL of each filler-loading was dropcast between pairs of thin-film Au electrodes, with a total of four samples for each mixture. The resistance across each sample was measured using the two-point probe method. A source-meter (Keithley 2460) was used to supply a potential across a pair of needle-tip electrodes mounted to probe positioners (J Micro Technologies, KRN-09S) attached to a probe station. DC linear voltage sweeps were applied across each sample, typically ranging from −500 mV–500 mV at a step potential of 10 mV and an integration time of 2 s. Ohmic I–V curves were obtained. No appreciable variation in conductivity was observed due to minor variations in thin-film Au electrode thickness as shown in Fig. S1–S3 (ESI†).

Surface hydrophobization

Two separate composite devices of the same composition and filler-loading were used to investigate the effects of surface hydrophobization on the electronic properties of the prepared MWCNT/PU composites, as well as to determine the wettability of hydrophobically modified composite surfaces. For constructing a containment well to serve as a dropcast mold, PET masks were cut to size and placed onto pristine glass substrates (Corning 2947) with dimensions 2.5 cm × 2.5 cm × 1 mm. Masks were fixed to the glass substrates using double-sided tape such that they could be removed at a later time. A total of two PET masked glass slides, for both pristine and hydrophobically modified composite surfaces, were used to make sessile contact angle measurements. ~200 µL aliquots of a 25.2 wt% P-MWCNT/PU mixture were dropcast into the 1.5 cm × 1.5 cm PET well of each of the two sample substrates. TDFTS was selected as a hydrophobing agent in consideration of its highly non-polar organic substituents as well as its reactivity with respect to its three readily hydrolysable halogen moieties. Prior to CVD of TDFTS, any exposed surfaces other than the intended composite surfaces were tightly wrapped in low-density polytetrafluoroethylene tape. Samples to be treated with TDFTS vapor were then loaded onto a perforated disk suspended at the center of a sealed glass desiccator with the composite surface oriented upright and orthogonal to the local vertical. For each vapor treatment, ~4 mmol of TDFTS was pipetted into the bottom of the CVD chamber onto a smooth, clean glass surface. With the sample loaded inside, the chamber was sealed and placed in contact with a heat source set to maintain a temperature of ~100 °C at 1 atm. Following 20 min of vapor treatment, the heat source was shut off. The samples were left inside the CVD chamber in the absence of a heat source for an additional 20 min to allow any residual reactions to go to completion. During CVD, the evolution of HCl resulting from the hydrolysis of TDFTS serves as a catalyst, promoting further polycondensation reactions with both other hydrolyzed TDFTS molecules as well as with the substrate.

Condensation reactions with the surface of the MWCNT/PU composites are believed to occur between the hydrolyzed moieties of the TDFTS and hydroxyl groups decorating the nanocomposite/air interface resulting from residual unreacted hydroxyl groups intrinsic to the polyol components of the PU host matrix.

UV-Vis-NIR, Raman, and FTIR spectroscopy

A UV-Vis-NIR spectrometer (Ocean Optics HR 2000) with a deuterium/halogen light source (Ocean Optics DH-2000) was used to gain insight on the optical properties of the P-MWCNTs and O-MWCNTs used in assembling nanocomposites in this work. P-MWCNTs and O-MWCNTs were separately dispersed in DMF at a concentration of 10 μg mL^{-1}. Both solutions were briefly sonicated for 2 min under identical conditions. UV-Vis absorbance spectra were obtained by analyzing 3 aliquots of each solution in a quartz cuvette with an optical path length of 1 cm and averaging the resulting curves. Raman spectra of P-MWCNTs and O-MWCNTs were obtained using a micro-Raman system with a continuous wave laser operating at an excitation wavelength of 532 nm, a 40× objective lens, and a HORIBA iHR320 spectrometer equipped with a Synapse CCD. Samples were dispersed in ethanol and dropcast on a crystalline Si substrate for measurements. The average of 3 spectral curves were taken for each sample. Fourier transform-infrared (FTIR) spectra were obtained using a Bruker Optics ALPHA FTIR spectrophotometer in attenuated total reflection (ATR) mode outfitted with a ZnSe internal reflection element. FTIR spectra were obtained at 128 scans to average and a resolution of 2 cm^{-1}.

Field-emission scanning electron microscopy

Scanning electron micrographs were obtained using a Carl Zeiss LEO 1525 field-emission scanning electron microscope outfitted with a GEMINI field-emission column. Micrographs were obtained at accelerating potentials ranging from 2–10 kV and comparatively short working distances.

Thermogravimetric, differential calorimetric, and differential thermal analysis

Thermogravimetric, differential calorimetric, and differential thermal analysis were conducted using a TA Instruments SDT Q600. Linear ramping cycles from 25–600 °C under Argon at a flow rate of 50 mg mL^{-1} were measured in alumina pans.

Sessile contact angle measurements

All images captured for use in determining the sessile contact angles of MWCNT/PU composite surfaces were obtained using a high-definition optical microscope camera (Scienscope TrueColor USB 2.0) outfitted with a compound lens system (Scienscope MZ7 IF Lens and Video Coupler (1×)) analogous to a goniometer setup. Samples were placed on an adjustable leveled stage positioned 25 cm away from the front of the microscope lens system with a tungsten-halogen light source placed behind the sample aligned with and directed towards the camera through an optical fiber. A graduated syringe fastened to a clamp stand was used to deposit 50 μL of de-ionized (DI) water onto each of the four sides of each sample. Contact angle values were measured using ImageJ open source software running the LB-ADSA plugin, which processes an 8-bit image and determines the sessile contact angle by using first-order perturbation techniques to obtain solutions to the Young–Laplace equation.[87]

Effects of hydrophobization on the DC conductivity of submerged composites

The devices used to characterize these effects were fabricated using ITO-coated PET slides. These slides were cut to dimensions 15 cm × 1.9 cm, masked, then chemically etched using zinc powder and 6 N hydrochloric acid (aq.) to form pairs of electrodes with an interelectrode gap of ~500 μm. Samples of an 18.9 wt% O-MWCNT/PU composite were dropcast between pairs of ITO electrodes. Composites to be hydrophobically modified were subsequently wrapped with multiple layers of scotch tape, leaving only the composite surface exposed. These samples were then hydrophobically modified in the same manner as previously described. For electrical resistance measurements, the assembled devices were wrapped into a semicircle using scotch tape and a glass slide. A picoammeter/sourcemeter (Keithley 6487) with flat-faced clip electrodes attached near the ends of the device was used to pass a current through the composite samples. The composites were then submerged to a depth of 5 cm in DI water maintained at 19 °C contained within a transparent PMMA plastic reservoir and left unperturbed for 1 h. During this time, resistance measurements were taken at different time intervals. To eliminate extraneous sources of error, resistance measurements across pristine ITO-coated PET slides were taken for both planar and wrapped configurations in air as well as in DI water. No appreciable change in resistance due to submersion in DI water or wrapping of the ITO-coated PET slide was observed over a period of 1 h.

Conclusions

Highly electroconductive MWCNT/PU nanocomposites were assembled using an aqueous solvent-blending method. Low percolation thresholds of $p_{c_{\text{pristine}}} = 0.001$ wt% and $p_{c_{\text{oxidized}}} = 0.093$ wt% with corresponding critical values of $\tau_{\text{pristine}} = 2.067 \pm 0.094$ and $\tau_{\text{oxidized}} = 2.304 \pm 0.114$ were calculated for P-MWCNT/PU and O-MWCNT/PU composites, respectively. Saturated DC conductivities as high as 839 ± 72 S cm^{-1} were measured for O-MWCNT/PU composites at a high filler-loading of 30.9 wt%, which is attributed largely to the preservation of the large aspect ratios (350–500) of the MWCNTs used through minimal mechanical/chemical processing (*e.g.*, extended ultrasonication or harsh acid-treatment). In this work, the crossover region, where O-MWCNT/PU composites begin to exhibit higher conductivities than their P-MWCNT/PU analogs, occurs at comparatively high filler-loadings (~19 wt%). At such high MWCNT concentrations, entropy

favors higher probabilities for nanotube agglomeration/flocculation/bundling within the host matrix, corresponding to increased electron trap site formation. The authors reason that there exists a threshold beyond which the effects of higher, more uniform dispersion within the matrix outweigh the decrease in intrinsic conductivity resulting from oxygen-containing moieties along the exohedral surfaces introduced *via* chemical oxidation of pristine MWCNTs. More specifically, UV-Vis, Raman, and FTIR spectra strongly support the effects of the mild oxidation techniques implemented in this study. Oxidation of the outer surfaces of the MWCNTs used in this work irrevocably disrupt the sp²-hybridized conjugated electronic structure underpinning the high intrinsic conductance of such materials. The authors suggest that the macroscopically observable increase in DC conductivity of O-MWCNT/PU in comparison to P-MWCNT/PU are a manifestation of the improved interfacial interactions with the host polymer. In regards to electron transport mechanisms above percolation, at filler-loadings as high as ~19 wt%, transport is dominated by direct charge transfer across small ballistic tunneling junctions as opposed to electron hopping/tunneling mechanisms. This reasoning is supported by the FE-SEM micrographs of the ~10 wt% O-MWCNT/PU presented in this work.

Nanocomposite surfaces treated with the perfluoroalkylsilane TDFTS *via* CVD exhibited sessile contact angles as high as $\theta_{treated}$ = 154°, indicating the formation of a superhydrophobic surface. The transition from a hydrophilic to superhydrophobic state is attributed to both the intrinsic surface roughness of assembled nanocomposites at the MWCNT/PU–air interface and presence of the highly non-polar perfluoroalkyl moieties belonging to TDFTS molecules. From immersion testing, it was found that the increase in electrical resistance across untreated MWCNT/PU composites was greater than that across nanocomposites that were hydrophobically modified with TDFTS vapor by a factor of 3.56 after 1 h in DI water. This is a critical proof-of-concept that can be extrapolated towards developing more robust protective surface modification techniques for conductive polymeric composite materials susceptible to water absorption.

Conflicts of interest

There are no conflicts to declare.

Acknowledgements

References

1 H. Sirringhaus, *Adv. Mater.*, 2014, **26**, 1319–1335.

2 V. Podzorov, *Nat. Mater.*, 2013, **12**, 947–948.

3 Z. Chen, M. J. Lee, R. Shahid Ashraf, Y. Gu, S. Albert-Seifried, M. Meedom Nielsen, B. Schroeder, T. D. Anthopoulos, M. Heeney, I. McCulloch and H. Sirringhaus, *Adv. Mater.*, 2012, **24**, 647–652.

4 J. Mei, D. H. Kim, A. L. Ayzner, M. F. Toney and Z. Bao, *J. Am. Chem. Soc.*, 2011, **133**, 20130–20133.

5 W. Zhang, J. Smith, S. E. Watkins, R. Gysel, M. McGehee, A. Salleo, J. Kirkpatrick, S. Ashraf, T. Anthopoulos, M. Heeney and I. McCulloch, *J. Am. Chem. Soc.*, 2010, **132**, 11437–11439.

6 L. Schadler, *Nat. Mater.*, 2007, **6**, 257–258.

7 Y. Zhao, K. Thorkelsson, A. J. Mastroianni, T. Schilling, J. M. Luther, B. J. Rancatore, K. Matsunaga, H. Jinnai, Y. Wu, D. Poulsen, J. M. J. Frechet, A. Paul Alivisatos and T. Xu, *Nat. Mater.*, 2009, **8**, 979–985.

8 S. Iijima, *Nature*, 1991, **354**, 56–58.

9 R. M. Bagwell, J. M. McManaman and R. C. Wetherhold, *Compos. Sci. Technol.*, 2006, **66**, 522–530.

10 J.-M. Thomassin, C. Jérôme, T. Pardoen, C. Bailly, I. Huynen and C. Detrembleur, *Mater. Sci. Eng., R*, 2013, **74**, 211–232.

11 S.-t. Tan, M.-q. Zhang, M.-z. Rong and H.-m. Zeng, *Polym. Compos.*, 1999, **20**, 406–412.

12 J. Wang, Y. Chen, R. Li, H. Dong, Y. Ju, J. He, J. Fan, K. Wang, K.-S. Liao, L. Zhang, S. Curran and W. Blau, *J. Inorg. Organomet. Polym.*, 2011, **21**, 736–746.

13 K.-S. Liao, J. Wang, D. Früchtl, N. J. Alley, E. Andreoli, E. P. Dillon, A. R. Barron, H. Kim, H. J. Byrne, W. J. Blau and S. A. Curran, *Chem. Phys. Lett.*, 2010, **489**, 207–211.

14 P. M. Ajayan, O. Stephan, C. Colliex and D. Trauth, *Science*, 1994, **265**, 1212–1214.

15 S. A. Curran, J. Talla, S. Dias, D. Zhang, D. Carroll and D. Birx, *J. Appl. Phys.*, 2009, **105**, 073711.

16 K.-S. Liao, J. A. Talla, S. D. Yambem, D. Birx, G. Chen, F. Coldren, D. L. Carroll, L. Ci, P. M. Ajayan, D. Zhang and S. A. Curran, *J. Mater. Res.*, 2010, **25**, 1741–1747.

17 J. N. Coleman, S. Curran, A. B. Dalton, A. P. Davey, B. McCarthy, W. Blau and R. C. Barklie, *Phys. Rev. B: Condens. Matter Mater. Phys.*, 1998, **58**, R7492–R7495.

18 K. Z. Milowska, M. Ghorbani-Asl, M. Burda, L. Wolanicka, N. Ćatić, P. D. Bristowe and K. K. K. Koziol, *Nanoscale*, 2017, **9**, 8458–8469.

19 D. Janas, K. Z. Milowska, P. D. Bristowe and K. K. K. Koziol, *Nanoscale*, 2017, **9**, 3212–3221.

20 D.-X. Yan, H. Pang, B. Li, R. Vajtai, L. Xu, P.-G. Ren, J.-H. Wang and Z.-M. Li, *Adv. Funct. Mater.*, 2015, **25**, 559–566.

21 L.-C. Jia, D.-X. Yan, C.-H. Cui, X. Jiang, X. Ji and Z.-M. Li, *J. Mater. Chem. C*, 2015, **3**, 9369–9378.

22 Z. Lv, C.-L. Jia, X. Ji, D.-X. Yan, J. Lei and Z.-M. Li, *J. Mater. Chem. C*, 2018, **6**, 12955–12964.

23 S. Paul, Y. S. Kang, J.-H. Yim, K. Y. Cho and D.-W. Kim, *Curr. Appl. Phys.*, 2010, **10**, e101–e104.

24 S. Azoz, L. M. Gilbertson, S. M. Hashmi, P. Han, G. E. Sterbinsky, S. A. Kanaan, J. B. Zimmerman and L. D. Pfefferle, *Carbon*, 2015, **93**, 1008–1020.

25 M. Shimizu, S. Fujii, T. Tanaka and H. Kataura, *J. Phys. Chem. C*, 2013, **117**, 11744–11749.

26 J. E. M. Marcelino, E. V. Santiago, G. Lopez-Tellez and S. H. López, *J. Nano Res.*, 2014, **28**, 51–61.

27 H. J. Park, M. Park, J. Y. Chang and H. Lee, *Nanotechnology*, 2008, **19**, 335702.

28 E. Andreoli, K.-S. Liao, A. Cricini, X. Zhang, R. Soffiatti, H. J. Byrne and S. A. Curran, *Thin Solid Films*, 2014, **550**, 558–563.

29 S. A. Curran, P. M. Ajayan, W. J. Blau, D. L. Carroll, J. N. Coleman, A. B. Dalton, A. P. Davey, A. Drury, B. McCarthy, S. Maier and A. Strevens, *Adv. Mater.*, 1998, **10**, 1091–1093.

30 D. K. Chattopadhyay and K. V. S. N. Raju, *Prog. Polym. Sci.*, 2007, **32**, 352–418.

31 J. U. Lind, T. A. Busbee, A. D. Valentine, F. S. Pasqualini, H. Yuan, M. Yadid, S.-J. Park, A. Kotikian, A. P. Nesmith, P. H. Campbell, J. J. Vlassak, J. A. Lewis and K. K. Parker, *Nat. Mater.*, 2017, **16**, 303–308.

32 G. Gumbs and D. Huang, *Properties of Interacting Low-Dimensional Systems (1)*, Wiley-VCH, Somerset, DE, 2013.

33 H. U. Lee, C. Park and J. Y. Park, *RSC Adv.*, 2016, **6**, 2149–2154.

34 Z. Zeng, M. Chen, H. Jin, W. Li, X. Xue, L. Zhou, Y. Pei, H. Zhang and Z. Zhang, *Carbon*, 2016, **96**, 768–777.

35 J. R. Bautista-Quijano, F. Avilés and J. V. Cauich-Rodriguez, *J. Appl. Polym. Sci.*, 2013, **130**, 375–382.

36 J. Kwon and H. Kim, *J. Polym. Sci., Part A: Polym. Chem.*, 2005, **43**, 3973–3985.

37 S. Yun, H. Im and J. Kim, *Synth. Met.*, 2011, **161**, 1361–1367.

38 Z. Zeng, H. Jin, M. Chen, W. Li, L. Zhou and Z. Zhang, *Adv. Funct. Mater.*, 2016, **26**, 303–310.

39 R. K. Crane and D. V. Rogers, *IEEE Trans. Antennas Propag.*, 2002, **50**, 1331–1332.

40 R. K. Crane, W. Xuhe, D. B. Westenhaver and W. J. Vogel, *Proc. IEEE*, 1997, **85**, 863–878.

41 X. F. Sanchez-Romate, A. Jimenez-Suarez, M. Sanchez, A. Guemes and A. Urena, *RSC Adv.*, 2016, **6**, 43418–43428.

42 N. K. Shrivastava and B. B. Khatua, *Carbon*, 2011, **49**, 4571–4579.

43 J. Li, P. C. Ma, W. S. Chow, C. K. To, B. Z. Tang and J. K. Kim, *Adv. Funct. Mater.*, 2007, **17**, 3207–3215.

44 J. N. Coleman, A. Fleming, S. Maier, S. O'Flaherty, A. I. Minett, M. S. Ferreira, S. Hutzler and W. J. Blau, *J. Phys. Chem. B*, 2004, **108**, 3446–3450.

45 S. Giordani, S. D. Bergin, A. Drury, É. N. Mhuircheartaigh, J. N. Coleman and W. J. Blau, *AIP Conf. Proc.*, 2005, **786**, 232–235.

46 B. E. Kilbride, J. N. Coleman, J. Fraysse, P. Fournet, M. Cadek, A. Drury, S. Hutzler, S. Roth and W. J. Blau, *J. Appl. Phys.*, 2002, **92**, 4024–4030.

47 A. Miller and E. Abrahams, *Phys. Rev.*, 1960, **120**, 745–755.

48 N. F. Mott, *J. Phys. C: Solid State Phys.*, 1980, **13**, 5433.

49 S. D. Kang and G. J. Snyder, *Nat. Mater.*, 2017, **16**, 252–257.

50 R. Noriega, J. Rivnay, K. Vandewal, F. P. V. Koch, N. Stingelin, P. Smith, M. F. Toney and A. Salleo, *Nat. Mater.*, 2013, **12**, 1038–1044.

51 L. C. Venema, J. W. G. Wildoer, J. W. Janssen, S. J. Tans, H. L. J. T. Tuinstra, L. P. Kouwenhoven and C. Dekker, *Science*, 1999, **283**, 52.

52 A. Rubio, D. Sánchez-Portal, E. Artacho, P. Ordejón and J. M. Soler, *Phys. Rev. Lett.*, 1999, **82**, 3520–3523.

53 L. A. Girifalco, M. Hodak and R. S. Lee, *Phys. Rev. B: Condens. Matter Mater. Phys.*, 2000, **62**, 13104–13110.

54 W. S. Bao, S. A. Meguid, Z. H. Zhu and G. J. Weng, *J. Appl. Phys.*, 2012, **111**, 093726.

55 J. G. Simmons, *J. Appl. Phys.*, 1963, **34**, 1793–1803.

56 N. Zettili, *Quantum mechanics : concepts and applications*, Wiley, Chichester, England, New York, 2001.

57 N. W. Ashcroft and D. N. Mermin, *Solid State Physics*, Holt, Rinehart and Winston, New York, 1976.

58 T. Hertel, R. E. Walkup and P. Avouris, *Phys. Rev. B: Condens. Matter Mater. Phys.*, 1998, **58**, 13870–13873.

59 S. Gong, Z. H. Zhu and E. I. Haddad, *J. Appl. Phys.*, 2013, **114**, 074303.

60 Y. Wang, G. J. Weng, S. A. Meguid and A. M. Hamouda, *J. Appl. Phys.*, 2014, **115**, 193706.

61 R. Saito, G. Dresselhaus and M. S. Dresselhaus, *Physical properties of carbon nanotubes*, World scientific, 1998.

62 H. J. Li, W. G. Lu, J. J. Li, X. D. Bai and C. Z. Gu, *Phys. Rev. Lett.*, 2005, **95**, 086601.

63 H. Kataura, Y. Kumazawa, Y. Maniwa, I. Umezu, S. Suzuki, Y. Ohtsuka and Y. Achiba, *Synth. Met.*, 1999, **103**, 2555–2558.

64 Y. Murakami and S. Maruyama, *Phys. Rev. B: Condens. Matter Mater. Phys.*, 2009, **79**, 155445.

65 M. S. Dresselhaus, G. Dresselhaus, R. Saito and A. Jorio, *Phys. Rep.*, 2005, **409**, 47–99.

66 J. Kastner, T. Pichler, H. Kuzmany, S. Curran, W. Blau, D. N. Weldon, M. Delamesiere, S. Draper and H. Zandbergen, *Chem. Phys. Lett.*, 1994, **221**, 53–58.

67 Y. Peng and H. Liu, *Ind. Eng. Chem. Res.*, 2006, **45**, 6483–6488.

68 S. M. Cakić, M. Špírková, I. S. Ristić, J. K. B-Simendić, M. M-Cincović and R. Poręba, *Mater. Chem. Phys.*, 2013, **138**, 277–285.

69 T. H. Scott, G. C. David, S. Sergei, X. Liping, O. Rahmi, B. Paul, U. Monica, S. S. Michael, S. Giles, S. Moonsub and K. Pawel, *Nat. Mater.*, 2003, **2**, 731.

70 P. Aminayi and N. Abidi, *Appl. Surf. Sci.*, 2013, **287**, 223–231.

71 S. R. Wasserman, Y. T. Tao and G. M. Whitesides, *Langmuir*, 1989, **5**, 1074–1087.

72 H. Hoffmann, U. Mayer and A. Krischanitz, *Langmuir*, 1995, **11**, 1304–1312.

73 G. Trovati, E. A. Sanches, S. C. Neto, Y. P. Mascarenhas and G. O. Chierice, *J. Appl. Polym. Sci.*, 2010, **115**, 263–268.

74 S. Zhang, Z. Ren, S. He, Y. Zhu and C. Zhu, *Spectrochim. Acta, Part A*, 2007, **66**, 188–193.

75 H. Kalita and N. Karak, *Polym. Int.*, 2014, **63**, 1295–1302.

76 D. Zavastin, I. Cretescu, M. Bezdadea, M. Bourceanu, M. Drăgan, G. Lisa, I. Mangalagiu, V. Vasić and J. Savić, *Colloids Surf., A*, 2010, **370**, 120–128.

77 H. A. Mohamed, B. M. Badran, A. M. Rabie and S. M. M. Morsi, *Prog. Org. Coat.*, 2014, **77**, 965–974.

78 D. L. Pugmire, C. J. Wetteland, W. S. Duncan, R. E. Lakis and D. S. Schwartz, *Polym. Degrad. Stab.*, 2009, **94**, 1533–1541.

79 S. Li, X. Du, C. Hou, X. Hao, J. Jia, T. Guan, T. Yi and G. Ma, *Compos. Sci. Technol.*, 2017, **143**, 46–55.

80 Z. Pan, H. Shahsavan, W. Zhang, F. K. Yang and B. Zhao, *Appl. Surf. Sci.*, 2015, **324**, 612–620.

81 Y. Ivanova, T. S. Gerganova, Y. Dimitriev, I. M. Miranda Salvado and M. H. V. Fernandes, *Thin Solid Films*, 2006, **515**, 271–278.

82 S. Pandey, S. K. Rath and A. B. Samui, *Ind. Eng. Chem. Res.*, 2012, **51**, 3531–3540.

83 C. Chiavari, A. Balbo, E. Bernardi, C. Martini, F. Zanotto, I. Vassura, M. C. Bignozzi and C. Monticelli, *Prog. Org. Coat.*, 2015, **82**, 91–100.

84 M. Y. L. Chew and X. Zhou, *Polym. Test.*, 2002, **21**, 187–193.

85 D. Ponnamma, K. K. Sadasivuni, M. Strankowski, Q. Guo and S. Thomas, *Soft Matter*, 2013, **9**, 10343–10353.

86 H. Luo, Y. Ma, W. Li, G. Yi, X. Cheng, W. Ji, X. Zu, S. Yuan and J. Li, *Mater. Lett.*, 2015, **161**, 189–192.

87 A. F. Stalder, T. Melchior, M. Müller, D. Sage, T. Blu and M. Unser, *Colloids Surf., A*, 2010, **364**, 72–81.